FULL PAPER

# $MoS_2$/Si Heterojunction with Vertically Standing Layered Structure for Ultrafast, High-Detectivity, Self-Driven Visible–Near Infrared Photodetectors

*Liu Wang, Jiansheng Jie,* Zhibin Shao, Qing Zhang, Xiaohong Zhang,* Yuming Wang, Zheng Sun, and Shuit-Tong Lee**

**As an interesting layered material, molybdenum disulfide ($MoS_2$) has been extensively studied in recent years due to its exciting properties. However, the applications of $MoS_2$ in optoelectronic devices are impeded by the lack of high-quality p–n junction, low light absorption for mono-/multilayers, and the difficulty for large-scale monolayer growth. Here, it is demonstrated that $MoS_2$ films with vertically standing layered structure can be deposited on silicon substrate with a scalable sputtering method, forming the heterojunction-type photodetectors. Molecular layers of the $MoS_2$ films are perpendicular to the substrate, offering high-speed paths for the separation and transportation of photo-generated carriers. Owing to the strong light absorption of the relatively thick $MoS_2$ film and the unique vertically standing layered structure, $MoS_2$/Si heterojunction photodetectors with unprecedented performance are actualized. The self-driven $MoS_2$/Si heterojunction photodetector is sensitive to a broadband wavelength from visible light to near-infrared light, showing an extremely high detectivity up to ≈$10^{13}$ Jones (Jones = cm $Hz^{1/2}$ $W^{-1}$), and an ultrafast response speed of ≈3 μs. The performance is significantly better than the photodetectors based on mono-/multilayer $MoS_2$ nanosheets. Additionally, the $MoS_2$/Si photodetectors exhibit excellent stability in air for a month. This work unveils the great potential of $MoS_2$/Si heterojunction for optoelectronic applications.**

## 1. Introduction

Graphene, a typical 2D material, has aroused tremendous attention due to its outstanding electronic, optical, and mechanical properties.[1–5] However, the semi-metal properties with zero bandgap of graphene have restricted its applications in electronic and optoelectronic devices, which require semiconductor materials with nonzero bandgap.[6] Recently, other kinds of 2D materials such as layered metal dichalcogenides have attracted much research interest due to their excellent electronic and optical properties, as well as nonzero band gap.[7–9] Molybdenum disulfide ($MoS_2$), a typical 2D metal dichalcogenide, exhibits a direct bandgap of 1.8 eV in monolayer and an indirect bandgap of 1.3 eV for bulk or multilayer.[10,11] It shows a high carrier mobility of ≈200 $cm^2$ $V^{-1}$ $s^{-1}$ for monolayer and ≈500 $cm^2$ $V^{-1}$ $s^{-1}$ for few layers.[12,13] More importantly, the light absorption of $MoS_2$ spans from visible to near-infrared spectral region (350–950 nm),[14] and reaches 5–10% of incident sunlight in a thickness of less than 1 nm, achieving one order of magnitude higher sunlight absorption than GaAs and Si.[15] Based on these appealing properties, $MoS_2$ has found important applications in various fields, such as catalysis,[16,17] nanoelectronics,[18,19] light harvesting,[20,21] and photovoltaics.[22–24] For instance, 200 nm thick $MoS_2$ membrane stacked with Au forms a Schottky-barrier solar cell to achieve a power conversion efficiency of 1.8%.[14] The thinnest photovoltaic devices were developed from the $MoS_2$/graphene and $WS_2$/$MoS_2$ stacked monolayers, which showed power conversion efficiencies of 1%, corresponding to one to three orders of magnitude higher power densities than the existing solar cells.[15,25]

As a key component for the nano-optoelectronic system, photodetectors based on semiconductor nanostructures have attracted much attention.[26,27] For practical applications, e.g., imaging and optical communication, fast response speed and high sensitivity of the photodetectors are much desirable.[28] Though photodetectors with remarkable speed and sensitivity have been developed from various 1D nanostructures, such as ZnSe,[29] CdS,[30] GaN[31] nanowires and nanoribbons, the inherent difficulties of 1D nanostructures in device integration impede their wide applications. In contrast, 2D layered materials offer the great promise of fabricating high-performance photodetectors for large-scale applications. To date, photodetectors based on mono-/multilayer $MoS_2$ or $MoS_2$/graphene hybrid

L. Wang, Prof. J. S. Jie, Dr. Z. B. Shao, Q. Zhang, Prof. X. H. Zhang, Y. M. Wang, Z. Sun, Prof. S.-T. Lee
Institute of Functional Nano and Soft Materials (FUNSOM)
Collaborative Innovation Center of Suzhou Nano Science and Technology
Jiangsu Key Laboratory for Carbon-Based Functional Materials and Devices
Soochow University
Suzhou, Jiangsu 215123, P. R. China
E-mail: jsjie@suda.edu.cn; xhzhang@mail.ipc.ac.cn; apannale@suda.edu.cn

DOI: 10.1002/adfm.201500216

**Table 1.** Performance comparison of our $MoS_2$/Si heterojunction-based photodetector with the $MoS_2$-based photodetectors in literatures.

| Device | Measurement condition (wavelength, bias) | Detectivity [cm $Hz^{1/2}$ $W^{-1}$] | Rise time [μs] | Fall time [μs] | Ref. |
|---|---|---|---|---|---|
| $MoS_2$/Si heterojunction | 808 nm, $V = 0$ V | $\approx 10^{13}$ | ≈3 | ≈40 | This work |
| $MoS_2$ p–n diode | 500 nm, $V = 1.5$ V | $3 \times 10^{10}$ | $1.5 \times 10^5$ | _ | [63] |
| Monolayer $MoS_2$ phototransistor | 561 nm, $V_{DS}$[a)] = 8 V, $V_G$[b)] = −70 V | _ | $4 \times 10^6$ | $9 \times 10^6$ | [34] |
| Multilayer $MoS_2$ phototransistor | 532 nm, $V_{DS} = 10$ V, $V_G = 0$ V | $\approx 10^{10}$ | 70 | 110 | [32] |
| $MoS_2$–graphene hybrid phototransistor | 632.8 nm, $V_{DS} = 0.1$ V, $V_G = 0$ V | _ | $2.8 \times 10^5$ | $1.5 \times 10^6$ | [33] |
| $MoS_2$/a-Si heterojunction | 550 nm, $V = 1$ V | _ | 300 | 300 | [43] |

[a)]The voltage applied on drain and source electrodes; [b)]The voltage applied on gate electrode.

structure have been intensively studied.[32–34] They show excellent device characteristics in terms of high sensitivity and wide band response. However, because of the absence of high-quality p–n junctions, $MoS_2$-based photodetectors still suffer from low detectivity ($10^8$–$10^{10}$ Jones) (Jones = cm $Hz^{1/2}$ $W^{-1}$) and slow response speed (70–$10^6$ μs).[32–34] On the other hand, monolayer or multilayer $MoS_2$ can only absorb a small portion of incident light due to the small thickness, thus restricting photocurrent improvement. Differing from graphene, which can be attained in large-area through catalytic growth on metal substrates,[35] large-area growth of intact monolayer $MoS_2$, e.g., in square centimeter size, has not yet been widely demonstrated,[36] making it difficult to utilize the monolayer $MoS_2$ for large-scale device applications.

In comparison to the formation of homojunctions or heterojunctions, respectively, from one or two different 2D layered materials,[33,37] the formation of heterojunctions by combining a 2D layered material with a semiconductor offers a feasible and easier way to construct high-performance optoelectronic devices by harnessing the advantages of both materials.[38,39] Taking graphene as an example, the fabrication of graphene/crystalline silicon (c-Si) heterojunctions has yielded high-efficiency solar cells (>10%) and ultrafast photodetectors with 40 GHz band.[28,35,40–42] The high-quality junction, along with the strong built-in electric field at the junction, is suggested to be responsible for the extraordinary device performance of the graphene/Si heterojunctions. However, up to now, there are few reports on $MoS_2$/Si heterojunctions due to the difficulty in the growth of large-area intact monolayer $MoS_2$. Salahuddin et al. reported the fabrication of heterojunction photodetectors consisting of 60 nm thick mechanically exfoliated $MoS_2$ flake and 100 nm amorphous silicon (a-Si).[43] Despite the high responsivity of 210 mA $W^{-1}$, the device exhibited a slow response speed of 0.3 ms due to structural defects in a-Si. Therefore, compared to the graphene/Si devices, there is a large room for the improvement of the $MoS_2$/Si heterojunction devices.

Herein, we report the construction of $MoS_2$/c-Si heterojunctions and their applications as high-sensitivity, ultrafast, self-driven visible-near infrared (NIR) photodetectors. Large-area $MoS_2$ film with a distinct vertically standing layered structure was deposited by using a facile and scalable magnetron sputtering method. The light absorption of the $MoS_2$ film was remarkably enhanced due to the large film thickness, whereas the vertically standing layered structure greatly facilitated the transport of photo-generated carriers along the in-plane direction to the top collection electrode. Significantly, the $MoS_2$/Si heterojunctions exhibited pronounced photovoltaic activity, enabling their applications as self-driven photodetectors operated at zero bias voltage. The self-driven $MoS_2$/Si photodetectors showed excellent characteristics in terms of wide photoresponse range of 450–1050 nm, ultrafast response speed of ≈3 μs, extremely high detectivity of $\approx 10^{13}$ Jones, and robust environmental stability. The performance characteristics have largely surpassed those reported for $MoS_2$-based photodetectors, as shown in **Table 1**. It is expected that the $MoS_2$/Si heterojunctions will have important applications in high-performance optoelectronic devices.

## 2. Results and Discussion

**Figure 1**a illustrates the X-ray diffraction (XRD) patterns of the sputter-deposited $MoS_2$ film on the Si substrate with a thickness of approx. 150 nm. The film size is 2 cm × 2 cm (inset in Figure 1a). Large-size $MoS_2$ film can be readily obtained by increasing the sizes of substrate and $MoS_2$ target. Post-annealing at 800 °C in Ar for 10 min was conducted to further improve the crystal quality of the film. All the diffraction peaks in the patterns can be indexed to $MoS_2$ with a hexagonal phase (JCPDS Card No. 75-1539). The as-prepared $MoS_2$ film shows a relatively strong (100) peak and a broadened (110) peak. After annealing, the intensities of the diffraction peaks are remarkably enhanced, along with the appearance of new peaks for (103) and (200) faces, indicating that the crystallinity of the film is improved. The $MoS_2$ film has a polycrystalline structure, whereas the strong (100) and (200) peaks disclose the preferential [100] orientation of the film on the Si substrate. Raman spectra were measured to investigate the crystal structures of the $MoS_2$ film, as shown in Figure 1b. Prior research indicates that there is a significant difference in the scattering modes of Raman spectra for $MoS_2$ nanosheets with different layer numbers. $MoS_2$ nanosheets usually show two strong signals from in-plane $E^1_{2g}$ and out-of-plane $A_{1g}$ vibrations. The $E^1_{2g}$ vibration tends to red-shift, whereas the $A_{1g}$ vibration tends to blue-shift, with an increasing $MoS_2$ layer number,[44,45] which enables the determination of the layer number from the difference of these two vibrations. As a thick $MoS_2$ film (approx. 150 nm) was adopted in this work to enhance light absorption, the Raman spectra are more likely to be identical to that of the $MoS_2$ bulk material. In Figure 1b, two dominant Raman modes at wave

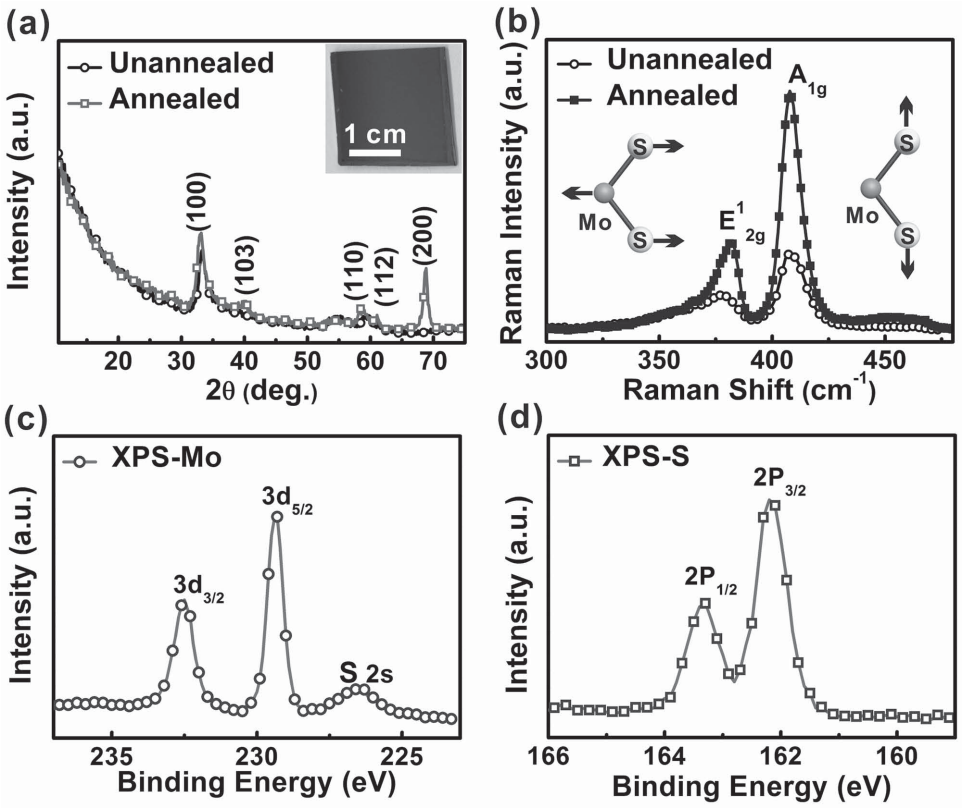


**Figure 1.** a) XRD patterns. b) Raman spectra of both as-prepared and annealed $MoS_2$ films. Inset in (a) shows the photograph of an annealed sample of 150 nm $MoS_2$ film on Si substrate. Schematic illustrations in (b) depict the atomic vibration direction of $E^1_{2g}$ (left) and $A_{1g}$ (right) Raman modes of $MoS_2$. XPS spectra show the binding energies of c) Mo and d) S for the annealed $MoS_2$ film.

numbers of 382 and 408 $cm^{-1}$, respectively, can be identified. This result is consistent with the previous report and the Raman modes can be assigned to the $E^1_{2g}$ and $A_{1g}$ modes of a thick $MoS_2$ film, respectively.[9,14] After annealing, the peak intensities are remarkably improved, whereas the peak width is decreased, revealing the superior crystallinity of the annealed film. X-ray photoemission spectroscopy (XPS) analysis was conducted to determine the components and binding energies of the annealed $MoS_2$ film (Figure 1c,d). The peaks at 229.3 and 232.5 eV are related to Mo $3d_{5/2}$ and Mo $3d_{3/2}$ orbitals, respectively, whereas S $2p_{3/2}$ and S $2p_{1/2}$ orbitals of divalent sulfide ions ($S^{2-}$) are observed at 162.2 and 163.3 eV, respectively. The results are in good agreement with the reported values for the $MoS_2$ crystal.[46–48]

**Figure 2**a depicts the schematic illustration of the $MoS_2$/Si heterojunction photodetector. The $MoS_2$ film was deposited on the p-Si substrate with a predefined $SiO_2$ window via magnetron sputtering, so that the effective device area could be precisely determined by the window size (3 mm × 3 mm). A 50 nm Ag electrode was used as the top contact to $MoS_2$, whereas 50 nm Au served as the back contact to p-Si. To gain more insight into the structure of the $MoS_2$/Si heterojunction, a cross-sectional transmission electron microscopy (TEM) investigation was performed, as shown in Figure 2b–e. The $MoS_2$ film deposited by sputtering has a uniform thickness of approx. 150 nm (Figure 2b). From the energy dispersive X-ray spectroscopy (EDS) line-scanning analysis (Figure 2c) and the high-resolution TEM (HRTEM) image at the junction interface (Figure 2d), we can see that there is a thin $SiO_2$ interfacial layer (≈10 nm) between the Si substrate and the $MoS_2$ film. The thin $SiO_2$ layer is likely caused by oxidation of silicon during film deposition due to the residual oxygen in the deposition chamber. Interestingly, Figure 2b,d,e discloses that the $MoS_2$ film is polycrystalline with a vertically standing layered structure. The layer distance of ≈0.67 nm in the HRTEM images corresponds to the (001) face of $MoS_2$, and is in good agreement with the value for bulk $MoS_2$.[36,49,50] Differing from the mono-/multilayer $MoS_2$ films prepared by the conventional chemical vapour deposition method, in which the $MoS_2$ layers are usually lying on the substrate with (001) planes parallel to the substrate surface,[51–53] the molecular layers are perpendicular to the substrate for the sputter-prepared $MoS_2$ film. Each $MoS_2$ grain in the polycrystalline film consists of 12–20 $MoS_2$ monolayers and has a sectional area of 70–110 $nm^2$ (Figure 2f). Layered materials usually have a higher in-plane conductivity[12] and a much smaller out-of-plane conductivity because of the large layer distance and weak van der Waals force between adjacent layers.[50,54] For example, the weak out-of-plane interaction of graphene leads to out-of-plane electrical and thermal conductivities more than 1000 times lower than those of their in-plane analogues.[55] Therefore, we can expect that the distinct vertically standing layered structure of the $MoS_2$ film can greatly facilitate carrier transport from the junction interface to the top Ag electrode.

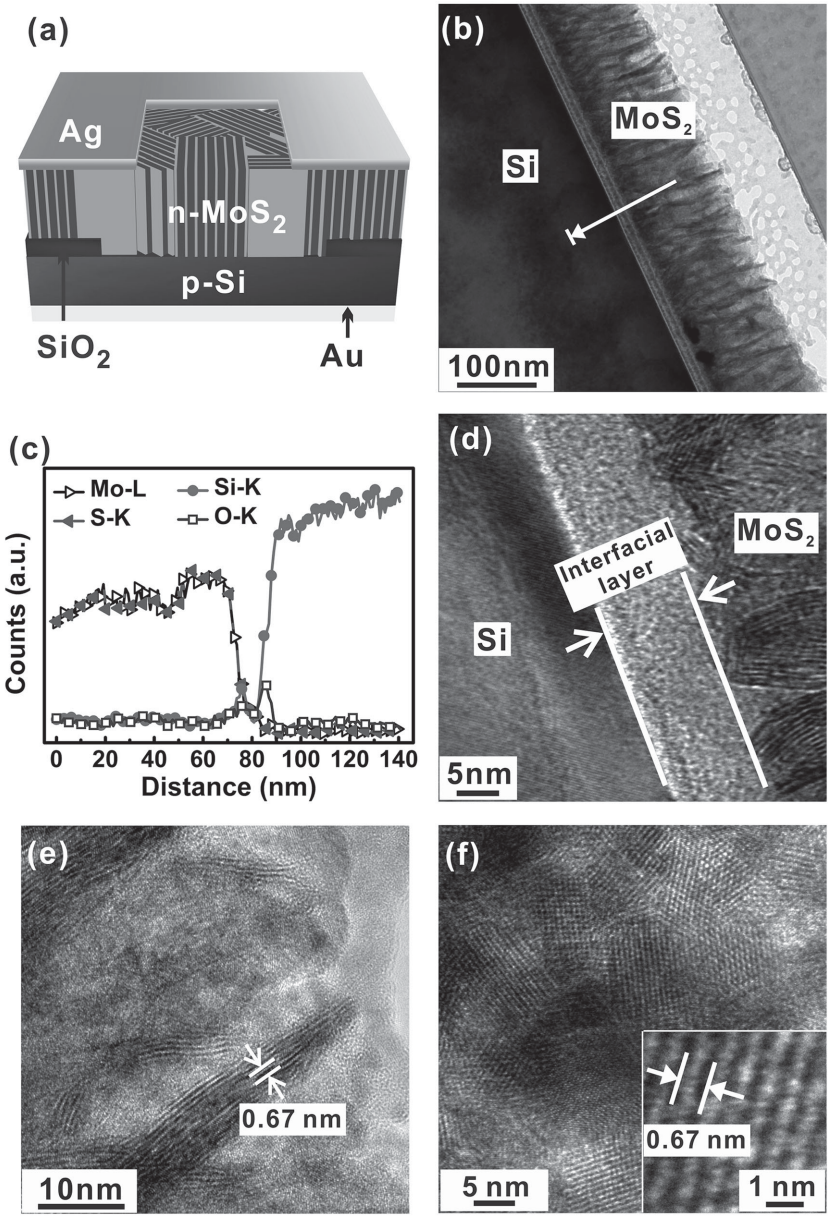


**Figure 2.** a) Schematic illustration of the $MoS_2$/Si heterojunction-based photodetector. b) Cross-sectional TEM image of the heterojunction. c) The line-scan EDS analysis along the red line from $MoS_2$ film to Si in (b). d) HRTEM image of the heterojunction, indicating the existence of an oxidation interfacial layer. e) HRTEM image of the $MoS_2$ film at the top surface. The distance between two layers is approx. 0.67 nm, corresponding to the (001) face of $MoS_2$. f) Top-view HRTEM image of the $MoS_2$ film, verifying that the $MoS_2$ film consists of many crystal domains. To facilitate the investigation, the film was directly deposited on the carbon-coated Cu grid by sputtering under the same conditions. The inset shows the enlarged HRTEM image.

To the best of our knowledge, this is the first demonstration of vertically standing layered $MoS_2$ films produced by using a magnetron sputtering method.

To directly evaluate the energy offset at the $MoS_2$/Si junction interface, the scanning Kelvin probe microscopy (SKPM) investigation was performed, as shown in **Figure 3**. Surface topographies in Figure 3a,b indicate that the $MoS_2$ film deposited by sputtering has a smooth surface. Notably, an evident potential difference between the $MoS_2$ film and the Si substrate is observed from the surface potential distributions (Figure 3c,d). Figure 3e shows the height and the potential profiles based on the data extracted from the cross-sections in Figure 3a,c. The potential of the Si substrate is higher than that of the $MoS_2$ film with a difference of approx. 100 meV. This result is in accordance with our anticipation that the work function of the p-type Si substrate should be larger than that of the n-type $MoS_2$ film. In this regard, the SKPM result provides a direct evidence for the existence of a junction barrier between the $MoS_2$ film and the Si substrate.

Figure 3f depicts the current versus voltage ($I$–$V$) characteristics of the $MoS_2$/Si p–n heterojunction in the dark. The effective device area is 9 $mm^2$. Significantly, the device exhibits an excellent rectifying behavior with a low-leakage current of approximately 0.0045 mA at −1 V and a high forward current of 23.34 mA at +1 V, yielding a high rectification ratio of 5000. The nearly linear $I$–$V$ curve of the Ag/$MoS_2$/Ag stacking structure in Figure S1 in Supporting Information proves that such a rectifying characteristic stems from the heterojunction between $MoS_2$ and Si, but not from the Ag/$MoS_2$ contact. The turn-on voltage is determined by extrapolating the $I$–$V$ curve to the intersection of the abscissa, giving rise to a small value of ≈0.25 V. In addition, the ideality factor ($n$) of the heterojunction could be deduced to be 1.83 from the slop of the semi-log $I$–$V$ curve in the forward bias direction, as shown in Figure S2 in Supporting Information, according to the following equation:[56]

$$n = \frac{q}{k_B T}\frac{dV}{d\ln I} \quad (1)$$

where $q$ is the unit charge, $k_B$ is the Boltzmann's constant, and $T$ is the absolute temperature. Though this value is somewhat larger than that for an ideal diode ($n$ = 1), it is very close to the optimized graphene/c-Si heterojunction solar cells in previous work ($n$ = 1.8, whose power conversion efficiencies under simulated AM 1.5 G solar irradiation could be as high as 10.56%).[35] Furthermore, the $I$–$V$ curve of the heterojunction in the dark could be described by thermionic emission theory of majority charge carriers over a potential zero bias barrier, $\Phi_b$, from the Si to $MoS_2$ film[57]

$$I = I_S\left[\exp\left(\frac{qV}{nk_B T}\right) - 1\right] \quad (2)$$

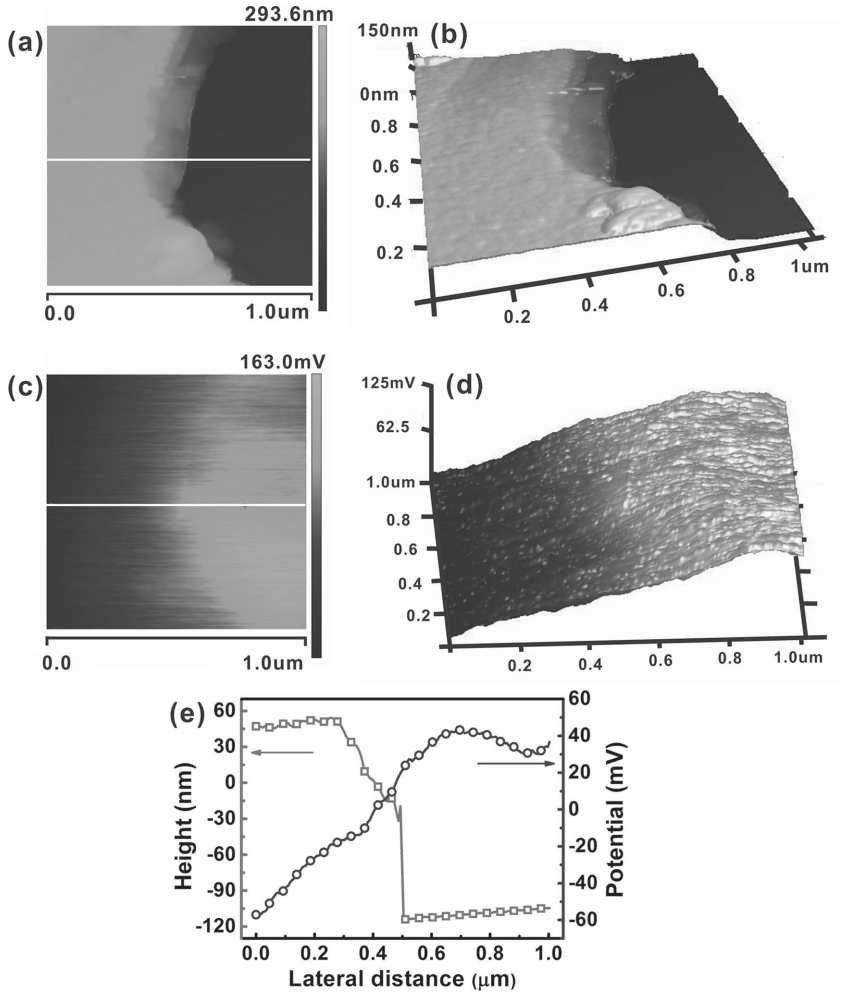


**Figure 3.** SKPM characterization of the $MoS_2$ film grown on the p-Si substrate. Surface topographies of the $MoS_2$/Si junction in a) 2D and b) 3D views. Surface potential distributions of $MoS_2$/Si junction in c) 2D and d) 3D views. e) Height and surface potential difference versus lateral profile across the $MoS_2$/Si interface along the white lines in (a) and (c). f) Typical *I–V* curves of the $MoS_2$/Si heterojunction in both linear and semi-log plots in the dark. The inset shows the photograph of the heterojunction-based photodetector.

The saturation current of $I_S$ is defined by

$$I_S = AA^*T^2\exp\left(-\frac{q\phi_b}{k_BT}\right) \quad (3)$$

where $A$ is the area of the device, $A^*$ is the effective Richadson constant, and it is 32 A cm$^{-2}$ K$^{-2}$ for p-type Si.[58]. Based on the above equations, $\Phi_b$ can be estimated to be approx. 330 meV. We note that the junction barrier height is larger than the value estimated from the SKPM measurement (approx. 100 meV). This is because the latter is more vulnerable to surface contamination or oxidation layer on the probe tip, leading to the underestimation of the barrier height. The high rectification ratio, low turn-on voltage, and small ideality factor unambiguously demonstrate the high quality of the heterojunction, thus offering a starting point for its applications in optoelectronic devices.

Next, we evaluated the photoresponse properties of the $MoS_2$/Si heterojunction. As shown in **Figure 4**a, the $MoS_2$/Si heterojunction exhibits an obvious photovoltaic activity under the illumination of an NIR 808 nm laser with a light intensity of 30 mW cm$^{-2}$; the photovoltage ($V_{ph}$) and photocurrent ($I_{ph}$) are deduced to be 210 mV and 100 μA, respectively. As we know, a photodetector with photovoltaic activity can operate without an external power. This kind of self-powered photodetector is, thus, a promising candidate for future devices aiming at reduced size and weight. From the photoresponse of the device at zero external bias voltage (Figure 4b), we note that the device shows high sensitivity to the incident 808 nm laser with a large $I_{on}/I_{off}$ ratio of $8 \times 10^3$. The steep rise and fall edges suggest a fast response speed, indicating that electron–hole pairs could be effectively generated and separated in the $MoS_2$/Si heterojunction. Also, the device possesses an excellent stability and reproducibility to pulsed light with about 23 s per cycle. The photoresponse characteristics can be further understood from the energy-band diagram illustrated in Figure 4c. Due to the difference in Fermi level ($E_F$), once the n-type $MoS_2$ film was deposited on the p-type Si substrate, electrons in $MoS_2$ film will tend to move to the Si side, whereas holes in Si will move to $MoS_2$ film. Therefore, the energy levels near the Si surface will bend downward whereas the energy levels near the $MoS_2$ surface will bend upward, eventually the Fermi levels of $MoS_2$ and Si align in the same level. As a result, a built-in electric field will present near the $MoS_2$/Si interface and has the direction from Si to $MoS_2$. Under light illumination, electron–hole pairs will be generated, which are then separated by the built-in electric field and collected by the electrodes, giving rise to photocurrent. The built-in electric field at the junction interface ensures that the device can operate at zero external bias voltage. Figure 4d plots the sensitivity of the photodetector as a function of wavelength. It can be seen that the present device exhibits a wide spectral response ranging from 450 to 1050 nm. The peak sensitivity is located at around 820 nm, which is in accordance with the absorption of $MoS_2$ film on the Si substrate (see Figure S3, Supporting Information), indicating that the incident light can be efficiently absorbed by the relatively thick $MoS_2$ layer. A 150 nm thick $MoS_2$ film was adopted in this investigation since it was the optimal thickness for the $MoS_2$/Si heterojunction photodetectors. Thinner $MoS_2$ film would lead to the reduction of light absorption, whereas thicker films would cause more defects-induced carrier recombination.

**Figure 5**a depicts the photoresponse characteristics of the heterojunction under the light illumination with varied wavelength. We kept the light intensity identical (10 mW cm$^{-2}$) for all wavelengths during testing. It is found that the photocurrent, along with the photovoltage, first increases with increasing wavelength from 420 to 808 nm, and then tends to

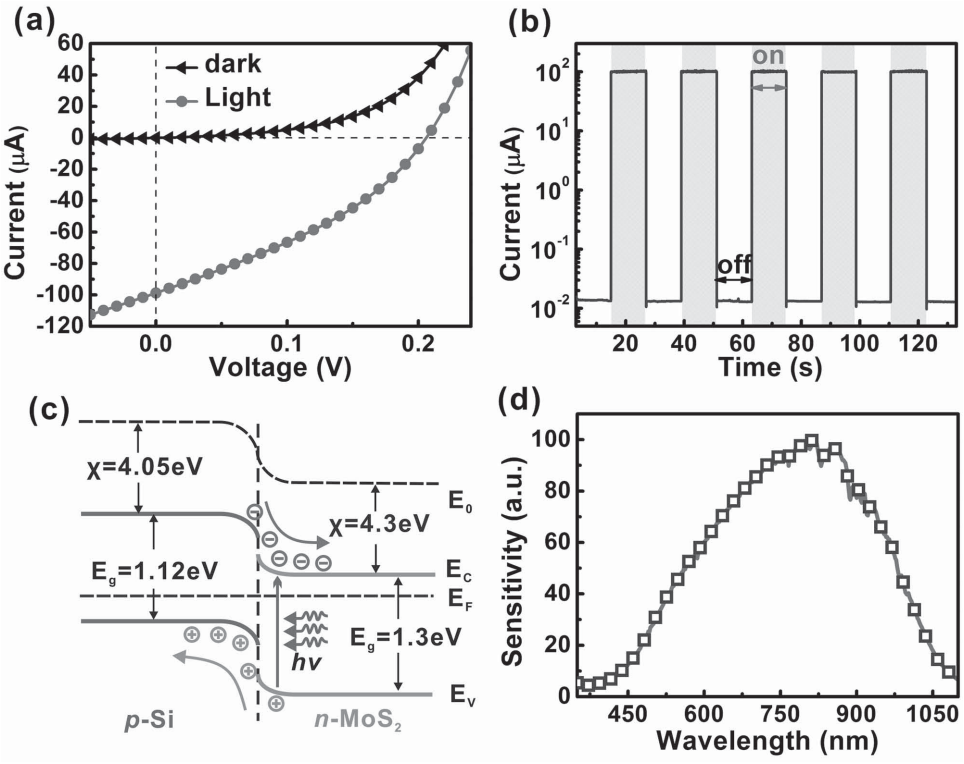


**Figure 4.** a) *I–V* characteristics of the $MoS_2$/Si heterojunction measured in the dark and under an NIR 808 nm laser (30 mW cm$^{-2}$) illumination, respectively. b) Photoresponse of the device under 808 nm laser illumination. The laser was turn on/off regularly to measure the time-dependent response of the photodetector. No external bias voltage was applied. c) Energy band diagram of the $MoS_2$/Si heterojunction under light illumination. The electron affinity ($\chi$) of p-Si and n-$MoS_2$ is 4.05 and 4.3 eV, respectively. The band gap ($E_g$) of p-Si and n-$MoS_2$ is 1.12 and 1.3 eV, respectively. $E_0$, $E_F$, $E_C$, and $E_V$ represent the vacuum energy level, Femi level, bottom of conduction band, and top of valence band, respectively. d) Spectral response of the heterojunction measured in the wavelength range 350–1100 nm.

decrease at longer wavelength. This tendency is consistent with the spectral response of the photodetector in Figure 4d. Moreover, we investigated the relationship of detection performance with light intensity, as shown in Figure 5b, by tuning the light intensity of the 808 nm laser from 1 to 30 mW cm$^{-2}$. One can see that both the photocurrent and the photovoltage highly depend on the light intensity and increase with increasing light intensity within the measurement range. Figure 5c shows that the photovoltage of the heterojunction increases rapidly from 144 to 202 mV when the light intensity changes from 1 to 20 mW cm$^{-2}$. However, further increase of the light intensity leads to saturation of the photovoltage. The maximum photovoltage of the device is supposedly determined by the Fermi level difference between $MoS_2$ and Si and is about 600 mV from the energy band diagram of the $MoS_2$/Si heterojunction in Figure 4c. It is larger than the measured photovoltage of the device, suggesting that the device performance may be further enhanced by optimizing the junction interface. The dependence of photocurrent on light intensity at zero external bias voltage is shown in the inset of Figure 5c. The curve can be well fitted with a power law, $I_P \sim P\theta$, where $\theta$ determines the response of the photocurrent to light intensity. The fitting gives an almost straight line with $\theta = 0.42$, which is smaller than that of low trap state junctions ($\theta \approx 1$),[39,59,60] implying the presence of some trap states between the Fermi level and the conduction band edge.[61]

Generally, the key figure-of-merit parameters of responsivity ($R$), detectivity ($D^*$), and response speed are used to evaluate the performance of a photodetector. Responsivity indicates how the efficiency of a detector responds to the optical signals and is given by the following equation:[21,37]

$$R = \frac{I_{ph}}{P_{in}} \tag{4}$$

where $P_{in}$ is the illumination power on the active area of the photodetector. Apparently, high responsivity indicates that a large photocurrent can be achieved under a relatively low optical input. On the other hand, detectivity represents the ability of a detector to detect weak optical signals. $D^*$ can be calculated from the following expression:[21,37]

$$D^* = \frac{A^{1/2}R}{(2qI_d)^{1/2}} = \frac{R}{(2qJ_d)^{1/2}} \tag{5}$$

where $I_d$ and $J_d$ represent the dark current and dark current density, respectively. It is assumed that the dark current is dominated by the shot noise for estimating detectivity.[21,37] Equation (5) suggests that a low dark current and a high responsivity are desired for the photodetector to achieve high detectivity. Based on Equation (4), responsivity of the $MoS_2$/Si heterojunction is estimated to be ≈300 mA W$^{-1}$ under a light

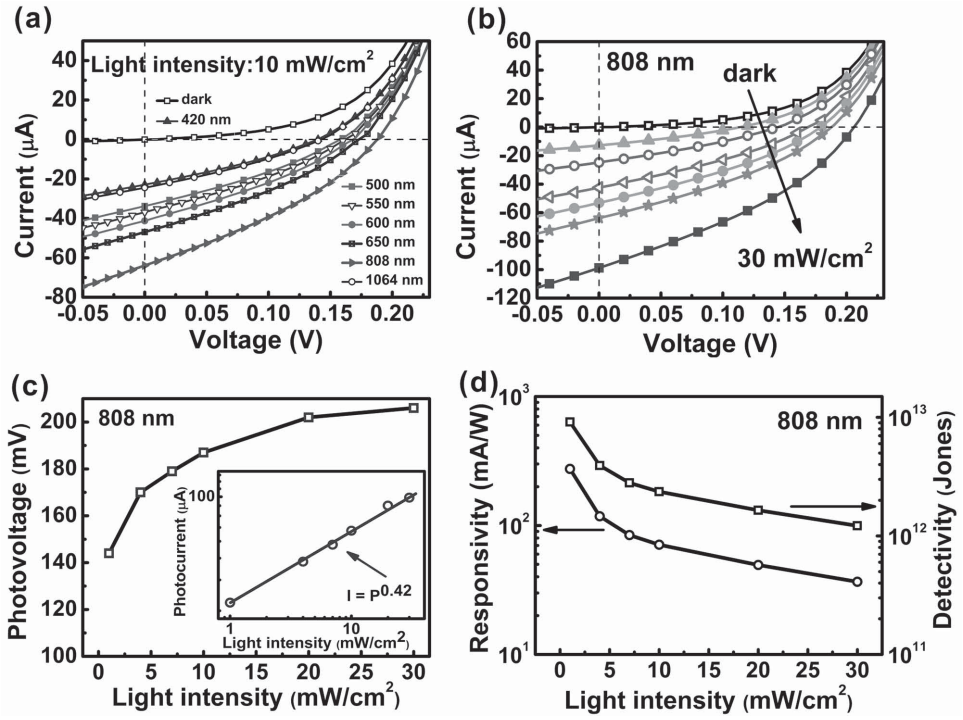


**Figure 5.** a) Photoresponse characteristics of the $MoS_2$/Si heterojunction measured under light illumination with different wavelengths. The light intensity was fixed at 10 mW $cm^{-2}$. b) Photoresponse characteristics of the heterojunction measured under 808 nm laser illumination with different light intensities. c) Photovoltage of the heterojunction as a function of light intensity. The inset shows the photocurrent at zero external bias voltage as a function of light intensity. The curve can be fitted according to power law. d) Plots of responsivity and detectivity as a function of light intensity.

intensity of 1 mW $cm^{-2}$, which is comparable to most of the reported values for $MoS_2$-based photodetectors.[21,32,62] However, significant improvement in detectivity has been investigated for the $MoS_2$/Si heterojunction; the value of $\approx 10^{13}$ Jones at 1 mW $cm^{-2}$ is three orders of magnitude higher than other $MoS_2$-based photodetectors (Table 1),[32,63,64] and is close to the Si p–n junction photodetector,[21,65], indicating that the $MoS_2$/Si heterojunction is extremely sensitive to small optical input signals. More importantly, such a high $D^*$ is acquired at zero external bias voltage, in contrast to the relatively high bias voltage needed in previous works.[33,37] Figure 5d plots the $R$ and $D^*$ of the $MoS_2$/Si heterojunction under zero bias voltage as a function of incident light intensity. We note that both $R$ and $D^*$ increase with the decrease of light intensity. Trap states in the $MoS_2$ layer or at the junction interface are suggested to be responsible for this phenomenon. Under weak light intensity, the photogenerated electrons in $MoS_2$ will be captured by the trap states. As a result of reduced recombination, the lifetime for the photogenerated holes can be greatly prolonged, leading to higher $R$ and $D^*$. However, the available states will be remarkably reduced with increasing light intensity, eventually causing the saturation of photoresponse.[33] Although different light intensities have been used in previous works, the $D^*$ in this work represents the highest value reported so far. The ultrahigh $D^*$ can be ascribed to the low dark current of the device, which is a characteristic of the junction-type photodetector, as well as the large photocurrent at zero external bias voltage.

Response speed is also one of the key figure of merits for a photodetector, particularly for that utilized in optical communication, imaging, and so on. In this work, we further investigate the response speed of the $MoS_2$/Si heterojunction photodetector by using an optical chopper to generate the pulsed light with varied frequency from 0 to 4000 Hz (**Figure 6**). The variation of photovoltage is then monitored by an oscilloscope to estimate the response speed. Figure 6a,b shows that the photoresponse of the heterojunction to the pulsed light is very fast with excellent long-term repeatability in the frequency range from 50 to 4000 Hz. Further study of the photovoltage as a function of frequency reveals a slow relative balance $(V_{max} - V_{min})/V_{max}$ decay (Figure 6c); the relative balance only decreases by less than 13% even at a high frequency of 4000 Hz, suggesting that the $MoS_2$/Si heterojunction photodetector can work well over a wide switching frequency range and is capable of monitoring ultrafast optical signals. From the magnified photoresponse curve in Figure 6e,f, a small rise time ($t_r$) and fall time ($t_f$) of 3 and 40 μs, respectively, can be estimated at zero external bias voltage. It is worth pointing out that this small response time is the best result achieved for the $MoS_2$-based photodetectors (Table 1). Furthermore, we investigated the air stability of the $MoS_2$/Si photodetector by placing it directly in air for a month without any encapsulation. The device showed remarkably high durability, and no obvious changes can be observed when the device was measured at 4000 Hz pulsed light again (see Figure S4a, Supporting Information). The $t_r$ ($t_f$) only slightly changes from 3 μs (40 μs) to 4 μs (42 μs) (Figure S4a,b, Supporting Information). The high stability of the device is directly related to the excellent air stability of $MoS_2$ film. Also, the $MoS_2$ film coating

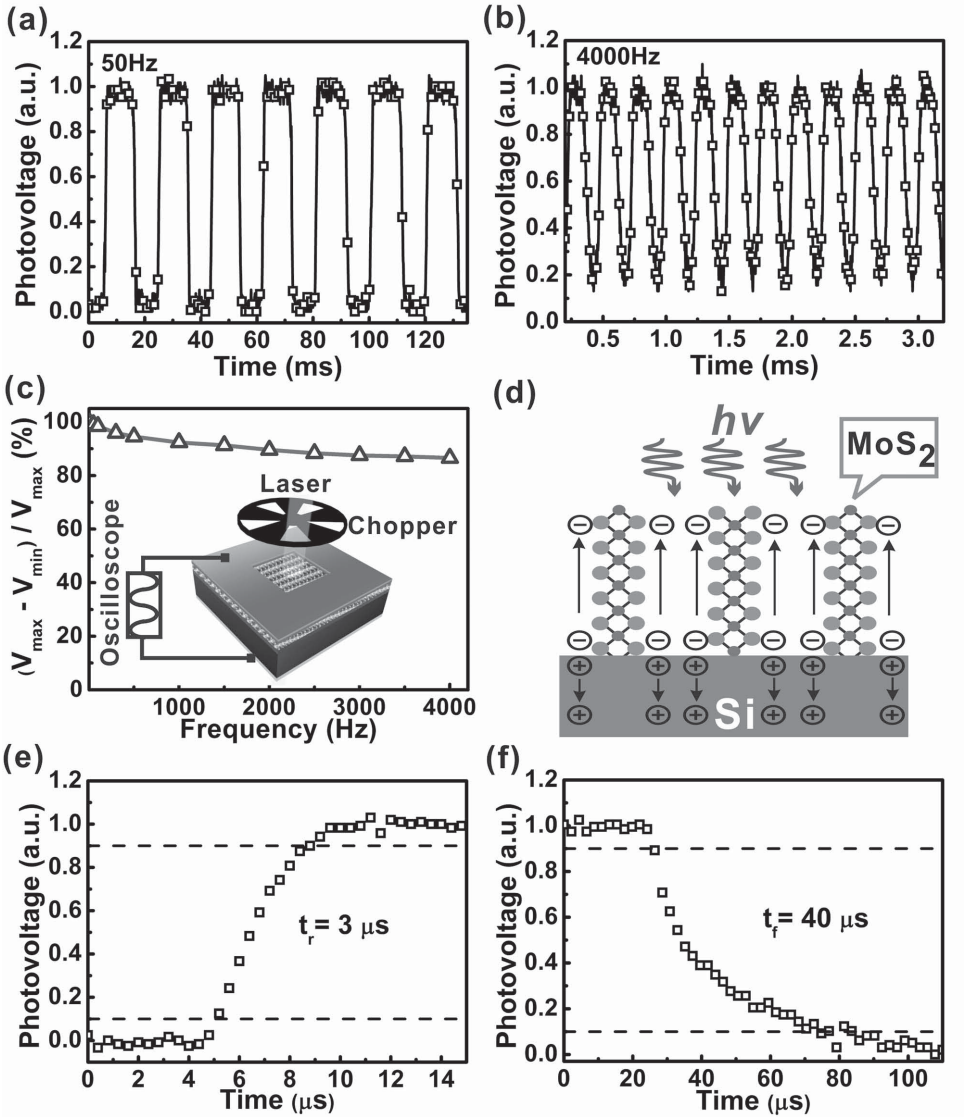


**Figure 6.** Photoresponse of the self-driven $MoS_2$/Si heterojunction photodetector to pulsed NIR light irradiation (808 nm laser) with a frequency of a) 50 Hz and b) 4000 Hz, respectively. c) Relative balance $(V_{max} - V_{min})/V_{max}$ versus switching frequency. The inset shows the schematic illustration of the setup for studying the time response of the photodetector. The variation of photovoltage is monitored by an oscilloscope. d) Schematic illustration shows the rapid separation and transportation of electrons and holes along the in-plane direction of $MoS_2$ during light illumination. e,f) show the enlarged rise and fall edges, respectively, of the photoresponse curve. The rise time ($t_r$) is the time interval for the response to rise from 10% to 90% of its peak value. The fall time ($t_f$) is the time interval for the response to decay from 90% to 10% of its peak value.

on the Si substrate can prevent further oxidation of Si in air and lead to high device stability. All the results demonstrate that the $MoS_2$/Si heterojunction photodetector can preserve high performance under air conditions for a long time, which is vital to the commercial photodetectors.

The high performance of the $MoS_2$/Si heterojunction photodetector could be ascribed to the following aspects: i) the existence of a strong build-in electric field at the $MoS_2$ and Si interface can greatly facilitate the separation and transport of photo-generated carriers, leading to the high response speed of the heterojunction. In contrast, in a conventional photoconductor-type photodetector, the response speed is limited by the transmit time of the carrier between the two ohmic contacts. The presence of carrier trapping centers also largely prolongs the response time of the photoconductor-type photodetector. ii) As shown in Figure 6d, due to the high in-plane mobility of the $MoS_2$ layer, the vertically standing layered structure of the $MoS_2$ layer offers high-speed paths for the transport of photogenerated carriers, resulting in a high response speed and large photocurrent. iii) From the TEM image in Figure 2d, a thin $SiO_2$ layer can be observed at the $MoS_2$ film and Si interface, which may serve as a passivation layer to reduce the interface defects, thus reducing the dark current and lessening the influence of interface defects on device performance.[66,67]

The above results clearly unveil the important role of heterojunction structure for enhancing the photoresponse properties of $MoS_2$. The sputtering method for generating the vertically standing layered $MoS_2$ films, as well as the unique device

structure design, is expected to be generally applicable to other 2D metal dichalcogenides such as $WS_2$ and $MoSe_2$, thus opening the opportunities for a variety of high-performance optoelectronic devices. Note that the power conversion efficiency for the self-powered $MoS_2$/Si heterojunction is ≈0.26% under a light intensity of 30 mW $cm^{-2}$, which is somewhat smaller than the previous reports for $MoS_2$ sheet-based solar cells.[14,15,24,25] The carrier recombination induced by the defects at the junction interface and in the bulk film is suggested to be responsible for the lower efficiency. Various improvements can be envisioned, such as improvement of the crystal quality of $MoS_2$ film by optimizing growth conditions and implementation of surface/interface passivation to reduce carrier recombination. In addition, as the response speed is related to the RC constant of the photodetector circuit; a larger active area of the device will result in a higher RC constant and consequently a lower response speed. Considering that a large device area of 9 $mm^2$ is used for the $MoS_2$/Si heterojunction photodetector, there is a large room for further improvement of the response speed by reducing the device size.

## 3. Conclusion

$MoS_2$/Si heterojunctions were fabricated by depositing $MoS_2$ films with a vertically standing layered structure on p-type silicon using the sputtering method. The $MoS_2$/Si heterojunction possessed a high rectification ratio of 5000, a low turn-on voltage of ≈0.25 V, and a small ideality factor of 1.83 in the dark, revealing the high quality of the heterojunction. The vertically standing layered $MoS_2$ film offers the advantages over the conventional mono-/multilayer $MoS_2$ nanosheets for optoelectronic applications in terms of strong light absorption and fast photogenerated carrier separation and transport. The heterojunction photodetector was able to operate at zero external bias voltage, thus minimizing the energy consumption and reducing the complexity of the external circuit design. As a result of high junction quality, the $MoS_2$/Si heterojunction photodetector exhibited a wide spectrum response ranging from visible to NIR light with an extremely high detectivity (≈$10^{13}$ Jones) and an ultrafast response speed (≈3 μs), which represent the best results achieved for $MoS_2$-based photodetectors thus far. In addition, the performance degradation of the device was nearly negligible after storing in air for a month. The development of the scalable sputtering method for vertically standing layered $MoS_2$ film deposition, along with the high device performance of the $MoS_2$/Si heterojunction, paves the way for high-performance $MoS_2$-based optoelectronic devices.

## 4. Experimental Section

*$MoS_2$ Film Deposition*: $MoS_2$ film with a vertically standing layered structure was deposited on the p-type Si substrate using magnetron sputtering (Kurt J Lesker, PVD 75). The 2 in. $MoS_2$ target was sintered by using $MoS_2$ power (Aldrich, purity 99%). The RF power, Ar gas pressure, and substrate temperature were controlled to be 50 W, 3 mTorr, and 400 °C, respectively, during sputtering. The deposition rate was approx. 2 nm $min^{-1}$, leading to a film thickness of 150 nm after a deposition time of 70 min. To improve the film crystallinity, the as-prepared $MoS_2$ films were annealed in Ar atmosphere at 800 °C for 10 min.

*Device Fabrication*: To fabricate the $MoS_2$/Si heterojunction, a photoresist window (3 mm × 3 mm) was first defined on the $SiO_2$ (300 nm)/p-type (100) Si (resistivity 1–10 Ω $cm^{-1}$) substrate by photolithography (SUSS, MicroTec-MJB4), and then the $SiO_2$ layer within the window was removed by dipping the substrate in a buffered oxide etch (BOE) solution for 300 s. After removing the residual photoresist in acetone for 5 min, 150 nm $MoS_2$ film was deposited according to the conditions mentioned above. Afterward, Ag (50 nm) top electrode and Au (50 nm) bottom electrode were deposited onto the $MoS_2$ film around the window position and the rear side of $SiO_2$/Si substrate, respectively, by e-beam evaporation (Kurt J Lesker, PVD 75). The pressure in the deposition chamber was approx. $5 \times 10^{-5}$ mTorr. The deposition rates for Ag and Au were controlled to be 0.3 Å $s^{-1}$.

*Characterizations of Materials and Devices*: Crystallinity and compositions of the $MoS_2$ films were characterized by using XRD (PANAlytical Empyrean), Raman spectroscopy (HORIBA JOBIN YVON, LabRAMHR800), XPS (Thermo ESCALAB 250), and line-scan EDX in HRTEM (JEOLJEM-2010). Interfacial structures and surface potential of the $MoS_2$/Si heterojunction were characterized by cross-sectional HRTEM and SKPM (Veeco, Multimode V), respectively. To evaluate the photoresponse characteristics of the heterojunctions, two light sources were used in the measurements: a Xe lamp with tuneable output power combined with a monochromator (Zolix Instruments, Omni-nx I) was used to produce the monochromatic light from visible light to NIR light range, whereas a 808 nm laser was used to offer a stronger light source at NIR light range. Electrical measurements were performed on a semiconductor characterization system (Keithley 4200-SCS). The response speed of the photodetector was evaluated by combining a light chopper and a digital oscilloscope (Tektronix TDS 2012C).

## Supporting Information

Supporting Information is available from the Wiley Online Library or from the author.

## Acknowledgements

This work was supported by the National Basic Research Program of China (Nos. 2013CB933500, 2012CB932400), the Major Research Plan of the National Natural Science Foundation of China (Nos. 91233110, 91333208), the National Natural Science Foundation of China (Nos. 51172151, 51173124), the Natural Science Foundation of Jiangsu Province (No. BK20131162), and a Project Funded by the Priority Academic Program Development of Jiangsu Higher Education Institutions. This work was sponsored by the Qing Lan Project.

Received: January 19, 2015
Revised: February 28, 2015
Published online: March 30, 2015

[1] Y. Zhu, S. Murali, W. Cai, X. Li, J. W. Suk, J. R. Potts, R. S. Ruoff, *Adv. Mater.* **2010**, *22*, 3906.
[2] X. M. Li, H. W. Zhu, K. L. Wang, A. .Y Cao, J. Q. Wei, C. Y. Li, Y. Jia, Z. Li, X. Li, D. H. Wu, *Adv. Mater.* **2010**, *22*, 2743.
[3] C. G. Lee, X. D. Wei, J. W. Kysar, J. Hone, *Science* **2008**, *321*, 385.
[4] A. C. Neto, F. Guinea, N. Peres, K. S. Novoselov, A. K. Geim, *Rev. Mod. Phys.* **2009**, *81*, 109.
[5] A. K. Geim, K. S. Novoselov, *Nat. Mater.* **2007**, *6*, 183.
[6] A. Castellanos-Gomez, E. Cappelluti, R. Roldán, N. Agraït, F. Guinea, G. Rubio-Bollinger, *Adv. Mater.* **2013**, *25*, 899.
[7] Q. H. Wang, K. Kalantar-Zadeh, A. Kis, J. N. Coleman, M. S. Strano, *Nat. Nanotech.* **2012**, *7*, 699.

[8] D. Chen, W. Chen, L. Ma, G. Ji, K. Chang, J. Y. Lee, *Mater. Today* **2014**, *17*, 184.
[9] X. Huang, Z. Y. Zeng, H. Zhang, *Chem. Soc. Rev.* **2013**, *42*, 1934.
[10] K. F. Mak, C. Lee, J. Hone, J. Shan, T. F. Heinz, *Phys. Rev. Lett.* **2010**, *105*, 136805.
[11] Y. Yoon, K. Ganapathi, S. Salahuddin, *Nano Lett.* **2011**, *11*, 3768.
[12] G. Eda, H. Yamaguchi, D. Voiry, T. Fujita, M. Chen, M. Chhowalla, *Nano Lett.* **2011**, *11*, 5111.
[13] B. Radisavljevic, A. Radenovic, J. Brivio, V. Giacometti, A. Kis, *Nat. Nanotechnol.* **2011**, *6*, 147.
[14] M. Shanmugam, C. A. Durcan, B. Yu, *Nanoscale* **2012**, *4*, 7399.
[15] M. Bernardi, M. Palummo, J. C. Grossman, *Nano Lett.* **2013**, *13*, 3664.
[16] D. Voiry, M. Salehi, R. Silva, T. Fujita, M. Chen, T. Asefa, V. B. Shenoy, G. Eda, M. Chhowalla, *Nano Lett.* **2013**, *13*, 6222.
[17] M. A. Lukowski, A. S. Daniel, F. Meng, A. Forticaux, L. Li, S. Jin, *J. Am. Chem. Soc.* **2013**, *135*, 10274.
[18] H. Wang, L. Yu, Y.-H. Lee, Y. Shi, A. Hsu, M. L. Chin, L.-J. Li, M. Dubey, J. Kong, T. Palacios, *Nano Lett.* **2012**, *12*, 4674.
[19] S. Das, H.-Y. Chen, A. V. Penumatcha, J. Appenzeller, *Nano Lett.* **2012**, *13*, 100.
[20] O. Lopez-Sanchez, E. A. Llado, V. Koman, A. F. Morral, A. Radenovic, A. Kis, *ACS Nano* **2014**, *8*, 3042.
[21] W. Choi, M. Y. Cho, A. Konar, J. H. Lee, G. B. Cha, S. C. Hong, S. Kim, J. Kim, D. Jena, J. Joo, *Adv. Mater.* **2012**, *24*, 5832.
[22] S. Wi, H. Kim, M. Chen, H. Nam, L. J. Guo, E. Meyhofer, X. Liang, *ACS Nano* **2014**, *8*, 5270.
[23] M. Fontana, T. Deppe, A. K. Boyd, M. Rinzan, A. Y. Liu, M. Paranjape, P. Barbara, *Sci. Rep.* **2013**, *3*, 1634.
[24] M.-L. Tsai, S. H. Su, J. K. Chang, D.-S. Tsai, C. H. Chen, C. I. Wu, L. J. Li, L. J. Chen, J. H. He, *ACS Nano* **2014**, *8*, 8317.
[25] L.-Y. Gan, Q. Zhang, Y. Cheng, U. Schwingenschlögl, *J. Phys. Chem. Lett.* **2014**, *5*, 1445.
[26] W. Tian, C. Zhang, T. Y. Zhai, S. L. Li, X. Wang, J. G. Liu, X. Jie, D. Q. Liu, M. Y. Liao, Y. Koide, D. Golberg,Y. Bando, *Adv. Mater.* **2014**, *26*, 3088.
[27] Y. P. Zhang, W. Deng, X. J. Zhang, X. W. Zhang, X. H. Zhang, Y. L. Xing, J. S. Jie, *ACS Appl. Mater. Interfaces* **2013**, *5*, 12288.
[28] T. Mueller, F. Xia, P. Avouris, *Nat. Photonics* **2010**, *4*, 297.
[29] X. W. Zhang, J. S. Jie, Z. Wang, C. Y. Wu, L. Wang, Q. Peng, Y. Q. Yu, P. Jiang, C. Xie, *J. Mater. Chem.* **2011**, *21*, 6736.
[30] J. S. Jie, W. J. Zhang, Y. Jiang, X. M. Meng, Y. Q. Li, S. T. Lee, *Nano Lett.* **2006**, *6*, 1887.
[31] H. Wu, Y. Sun, D. D. Lin, R. Zhang, C. Zhang, W. Pan, *Adv. Mater.* **2009**, *21*, 227.
[32] D.-S. Tsai, K. K. Liu, D.-H. Lien, M.-L. Tsai, C. F. Kang, C. A. Lin, L. J. Li, J. H. He, *ACS Nano* **2013**, *7*, 3905.
[33] H. Xu, J. H. Wu, Q. L. Feng, N. N. Mao, C. M. Wang, J. Zhang, *Small* **2014**, *10*, 2300.
[34] O. Lopez-Sanchez, D. Lembke, M. Kayci, A. Radenovic, A. Kis, *Nat. Nanotechnol.* **2013**, *8*, 497.
[35] C. Xie, X. Z. Zhang, Y. M. Wu, X. J. Zhang, X. W. Zhang, Y. Wang, W. J. Zhang, P. Gao, Y. Y. Han, J. S. Jie,*J. Mater. Chem. A* **2013**, *1*, 8567.
[36] Y. Zhan, Z. Liu, S. Najmaei, P. M. Ajayan, J. Lou, *Small* **2012**, *8*, 966.
[37] M. S. Choi, D. Qu, D. Lee, X. Liu, K. Watanabe, T. Taniguchi, W. J. Yoo, *ACS Nano* **2014**, *8*, 9332.
[38] H. T. Yu, S. Chen, X. F. Fan, X. Quan, H. M. Zhao, X. Y. Li, Y. B. Zhang, *Angew. Chem. Int. Ed.* **2010**, *49*, 5106.
[39] L. H. Zeng, M. Z. Wang, H. Hu, B. Nie, Y. Q. Yu, C. Y. Wu, L. Wang, J. G. Hu, C. Xie, F. X. Liang, L. B. Luo, *ACS Appl. Mater. Interfaces* **2013**, *5*, 9362.
[40] X. Z. Zhang, C. Xie, J. S. Jie, X. W. Zhang, Y. M. Wu, W. J. Zhang, *J. Mater. Chem. A* **2013**, *1*, 6593.
[41] X. Wang, Z. Cheng, K. Xu, H. K. Tsang, J. B. Xu, *Nat. Photon.* **2013**, *7*, 888.
[42] X. Gan, R.-J. Shiue, Y. Gao, I. Meric, T. F. Heinz, K. Shepard, J. Hone, S. Assefa, D. Englund, *Nat. Photonics* **2013**, *7*, 883.
[43] M. R. Esmaeili-Rad, S. Salahuddin, *Sci. Rep.* **2013**, *3*, 2345.
[44] C. Lee, H. Yan, L. E. Brus, T. F. Heinz, J. Hone, S. Ryu, *ACS Nano* **2010**, *4*, 2695.
[45] X. S. Wang, H. B. Feng, Y. G. Wu, L. Y. Jiao, *J. Am. Chem. Soc.* **2013**, *135*, 5304.
[46] K. K. Liu, W. Zhang, Y. H. Lee, Y. C. Lin, M. T. Chang, C. Y. Su, C. S. Chang, H. Li, Y. Shi, H. Zhang, C. S. Lai, L. J. Li, *Nano Lett.* **2012**, *12*, 1538.
[47] C. Altavilla, M. Sarno, P. Ciambelli, *Chem. Mater.* **2011**, *23*, 3879.
[48] K. Wong, X. Lu, J. Cotter, D. Eadie, P. Wong, K. Mitchell, *Wear* **2008**, *264*, 526.
[49] J. Kibsgaard, Z. Chen, B. N. Reinecke, T. F. Jaramillo, *Nat. Mater.* **2012**, *11*, 963.
[50] H. Ramakrishna Matte, A. Gomathi, A. K. Manna, D. J. Late, R. Datta, S. K. Pati, C. Rao, *Angew. Chem. Int. Ed.* **2010**, *122*, 4153.
[51] M. R. Laskar, L. Ma, S. Kannappan, P. S. Park, S. Krishnamoorthy, D. N. Nath, W. Lu, Y. Wu, S. Rajan, *Appl. Phys. Lett.* **2013**, *102*, 252108.
[52] Y. H. Lee, X. Q. Zhang, W. Zhang, M. T. Chang, C. T. Lin, K. D. Chang, Y. C. Yu, J. T. W. Wang, C. S. Chang, L. J. Li, T. W. Lin, *Adv. Mater.* **2012**, *24*, 2320.
[53] Y. Shi, W. Zhou, A. Y. Lu, W. Fang, Y. H. Lee, A. L. Hsu, S. M. Kim, K. K. Kim, H. Y. Yang, L. J. Li, J.-C. Idrobo, J. Kong, *Nano Lett.* **2012**, *12*, 2784.
[54] M. Chhowalla, G. A. Amaratunga, *Nature* **2000**, *407*, 164.
[55] M. J. Allen, V. C. Tung, R. B. Kaner, *Chem. Rev.* **2009**, *110*, 132.
[56] X. W. Zhang, X. J. Zhang, X. Z. Zhang, Y. P. Zhang, L. Bian, Y. M. Wu, C. Xie, Y. Y. Han, Y. Wang, P. Gao, L. Wang, J. S. Jie, *J. Mater. Chem.* **2012**, *22*, 22873.
[57] C. Xie, B. Nie, L. H. Zeng, F. X. Liang, M. Z. Wang, L. B. Luo, M. Feng, Y. Q. Yu, C. Y. Wu, Y. C. Wu, S. H. Yu, *ACS Nano*, **2014**, *8*, 4015.
[58] Ş. Karataş, Ş. Altındal, A. Türüt, A. Özmen, *Appl. Surf. Sci.* **2003**, *217*, 250.
[59] L. Li, E. Auer, M. Liao, X. Fang, T. Zhai, U. K. Gautam, A. Lugstein, Y. Koide, Y. Bando, D. Golberg, *Nanoscale* **2011**, *3*, 1120.
[60] D. Wu, Y. Jiang, Y. G. Zhang, J. W. Li, Y. Q. Yu, Y. P. Zhang, Z. F. Zhu, L. Wang, C. Y. Wu, L. B. Luo, J. S. Jie, *J. Mater. Chem.* **2012**, *22*, 6206.
[61] S.-C. Kung, W. E. van der Veer, F. Yang, K. C. Donavan, R. M. Penner, *Nano Lett.* **2010**, *10*, 1481.
[62] Z. Y. Yin, H. Li, H. Li, L. Jiang, Y. E. Shi, Y. G. Sun, G. Lu, Q. Zhang, X. D. Chen, H. Zhang, *ACS Nano* **2011**, *6*, 74.
[63] M. S. Choi, D. Qu, D. Y. Lee, X. Liu, K. Watanabe, T. Taniguchi, W. J. Yoo, *ACS Nano* **2014**, *8*, 9332.
[64] X. H. An, F. Z. Liu, Y. J. Jung, S. Kar, *Nano Lett.* **2013**, *13*, 909.
[65] X. Gong, M. H. Tong, Y. J. Xia, W. Z. Cai, J. S. Moon, Y. Cao, G. Yu, C.-L. Shieh, B. Nilsson, A. J. Heeger, *Science* **2009**, *325*, 1665.
[66] Y. Larionova, V. Mertens, N.-P. Harder, R. Brendel, *Appl. Phys. Lett.* **2010**, *96*, 032105.
[67] S. Olibet, E. Vallat-Sauvain, C. Ballif, *Phys. Lett. B* **2007**, *76*, 035326.